



HAL
open science

Monolithically integrated InGaAs/AlGaAs multiple quantum well photodetectors on 300 mm Si wafers

H. Mehdi, M. Martin, C. Jany, L. Viroth, J. Hartmann, J. da Fonseca, J. Moeyaert, P. Gaillard, J. Coignus, C. Leroux, et al.

► **To cite this version:**

H. Mehdi, M. Martin, C. Jany, L. Viroth, J. Hartmann, et al.. Monolithically integrated InGaAs/AlGaAs multiple quantum well photodetectors on 300 mm Si wafers. *AIP Advances*, 2021, 11 (8), pp.085028. 10.1063/5.0059237 . hal-03449032

HAL Id: hal-03449032

<https://hal.univ-grenoble-alpes.fr/hal-03449032v1>







Submitted on 6 Dec 2024

HAL is a multi-disciplinary open access archive for the deposit and dissemination of scientific research documents, whether they are published or not. The documents may come from teaching and research institutions in France or abroad, or from public or private research centers.

L'archive ouverte pluridisciplinaire **HAL**, est destinée au dépôt et à la diffusion de documents scientifiques de niveau recherche, publiés ou non, émanant des établissements d'enseignement et de recherche français ou étrangers, des laboratoires publics ou privés.

RESEARCH ARTICLE | AUGUST 24 2021

Monolithically integrated InGaAs/AlGaAs multiple quantum well photodetectors on 300 mm Si wafers

H. Mehdi ; M. Martin; C. Jany; L. Viro ; J. M. Hartmann; J. Da Fonseca; J. Moeyaert; P. Gaillard ; J. Coignus ; C. Leroux; C. Licitra ; B. Salem ; T. Baron  



AIP Advances 11, 085028 (2021)

<https://doi.org/10.1063/5.0059237>



View
Online



Export
Citation

Articles You May Be Interested In

Solar-blind ultraviolet emission-detection monolithic integration of AlGaN multiple-quantum-well diodes via concentric ring-circle configuration

Appl. Phys. Lett. (April 2024)

Micrometer-thick, atomically random $\text{Si}_{0.06}\text{Ge}_{0.90}\text{Sn}_{0.04}$ for silicon-integrated infrared optoelectronics

J. Appl. Phys. (November 2022)

Monolithically integrated photonic chips with asymmetric MQWs structure for suppressing Stokes shift

Appl. Phys. Lett. (January 2023)



Special Topics Open for Submissions

[Learn More](#)

Monolithically integrated InGaAs/AlGaAs multiple quantum well photodetectors on 300 mm Si wafers

Cite as: AIP Advances 11, 085028 (2021); doi: 10.1063/5.0059237

Submitted: 7 June 2021 • Accepted: 9 August 2021 •

Published Online: 24 August 2021



View Online



Export Citation



CrossMark

H. Mehdi,¹  M. Martin,¹ C. Jany,² L. Virost,²  J. M. Hartmann,² J. Da Fonseca,² J. Moeyaert,¹ P. Gaillard,^{1,2} 
J. Coignus,²  C. Leroux,² C. Licitra,²  B. Salem,¹  and T. Baron^{1,a)} 

AFFILIATIONS

¹ Univ. Grenoble Alpes, CNRS, CEA/LETI-Minatec, Grenoble INP (Institute of Engineering and Management Univ. Grenoble Alpes), LTM, F-38054 Grenoble, France

² Univ. Grenoble Alpes, CEA, LETI, Minatec Campus, F-38054 Grenoble Cedex, France

^{a)} Author to whom correspondence should be addressed: thierry.baron@cea.fr

ABSTRACT

Near infrared light detection is fundamental for sensing in various application fields. In this paper, we detail the properties of InGaAs/AlGaAs multiple quantum well (MQW) photodetectors (PDs) monolithically integrated by direct epitaxy on 300 mm Si(001) substrates. A MQW high crystalline quality is achieved using 300 mm Ge/Si pseudo-substrates with a low threading dislocation density of $4 \times 10^7 \text{ cm}^{-2}$ from electron channeling contrast imaging measurements. The localized states in the MQW stack are investigated using temperature-dependent photoluminescence. Two non-radiative recombination channels are identified. The first one is due to delocalized excitons generated by potential's fluctuations because of the InGaAs/AlGaAs interfacial roughness (with an activation energy below 4 meV). The second one is due to exciton quenching because of the presence of numerous threading dislocations. A low dark current density of $2.5 \times 10^{-5} \text{ A/cm}^2$ is measured for PDs on Ge/Si substrates, i.e., a value very close to that of the same PDs grown directly on GaAs(001) substrates. A responsivity of 36 mA/W is otherwise measured for the photodiode on Ge/Si at room temperature and at -2 V .

© 2021 Author(s). All article content, except where otherwise noted, is licensed under a Creative Commons Attribution (CC BY) license (<http://creativecommons.org/licenses/by/4.0/>). <https://doi.org/10.1063/5.0059237>

I. INTRODUCTION

Quantum well infrared photodetectors (QWIPs) have been extensively developed since the first observation of infrared transition (intersubband transition) in a GaAs QW embedded between two $\text{Al}_{0.3}\text{Ga}_{0.7}\text{As}$ barrier layers.¹ QWIPs with $\text{In}_x\text{Ga}_{1-x}\text{As}$ multiple quantum wells (MQWs) as active regions have a potential for mid-wave infrared (MWIR; 3 up to 5 μm band) and long-wave infrared (LWIR; 8 up to 12 μm band) detection. They are suitable for military and civilian applications in night vision cameras, thermal imaging systems, and medical imaging (neuroimaging, cancer detection, etc.). Intraband transitions in the QW, with electrons moving from one subband to another while remaining in the same band (conduction or valence band), must be used to cover these detection regions. Meanwhile, manipulating interband transitions in the QW enables near-wave infrared (NWIR; 0.7 up to 1 μm band) detection needed

for optical modulators,² multiband detectors,^{3,4} near-infrared spectroscopy (NIRS), and light detection and ranging (LIDAR) sensors for autonomous vehicles.⁵

Significant efforts have been made to integrate III-V optoelectronics devices on Si platforms using various methods, such as bonding, flip-chip integration, and direct epitaxial growth. Flip-chip integration is a costly and slow process as the alignment must be accurate for all III-V dies. Nowadays, direct wafer bonding is widely used to obtain new and innovative stacks. It has already been implemented industrially. More recently, monolithic III-V epitaxy on Si has gained much attention by researchers working on III-V photonics on Si, with significant progress made. Direct epitaxial growth of III-V layers on Si is indeed the method of choice for scalable and cost-efficient integration, the main challenge being to minimize the amount of structural defects in the active part of the devices. To overcome this challenge, many approaches have been explored,

such as (i) the insertion of superlattices combined with cyclic annealing and strain-balancing stacks on V-grooved Si substrates,^{6–8} (ii) template-assisted selective epitaxy (TASE),⁹ or (iii) the use of Si substrates buffered with GaP or Ge layers.^{10,11}

Modulator^{12–14} and photodetector (PD)^{15–18} devices based on strained InGaAs/AlGaAs or InGaAs/GaAs stacks on GaAs have been investigated for a long time, and their structures have been optimized. Alves *et al.*¹⁹ have fabricated GaAs/InGaAs quantum well PDs on GaAs for NIR band detection in the 825–940 nm wavelength range, with a high responsivity of 20 mA/W at 930 nm, at 10 K and under a 4.5 V bias. Katzer *et al.*²⁰ have investigated InGaAs/AlGaAs vertical PIN MQW optical modulators. They showed that indium concentrations less than 23% in those MQWs grown directly on GaAs resulted in better device performances than those with higher indium concentrations. Recently, significant efforts have been made to optimize QWIP and laser structures on Si.^{8,21–23} However, device performances still need to be further improved.

In this paper, we report on InGaAs/AlGaAs MQW photodetectors (PDs) monolithically integrated on GaAs(001) substrates, bare Si(001) substrates, and Ge-buffered Si(001) substrates. The vertical PIN design has been adapted to have room temperature light absorption in the direction parallel to the current collection. PDs have been fabricated and their performances have been evaluated. A correlation between the MQW physical properties and PD performances was made for each type of substrate. Our results show how the MQW quality affects the device operation and the potential of our approach to fabricate efficient PDs at large scales.

II. DEVICE FABRICATION

The structure of the PIN photodiode is shown in Fig. 1(a). Three MQW PIN structures were grown on *n*-type GaAs(001) substrates, bare Si(001) substrates, and Ge-buffered Si(001) substrates in a metal organic chemical vapor (MOCVD) reactor. *p*-type doped 300 nm Si(001) substrates with 0.15° or 0.5° miscuts toward one of the ⟨110⟩ directions were used to obtain Anti-Phase Boundary (APB)-free, single domain GaAs.²⁴ To prepare the Ge/Si pseudo-substrates, 1.6 μm thick Ge buffers were grown by chemical vapor

deposition at 90 Torr using GeH₄ in a separate group IV epitaxy tool. A low temperature (LT) (400 °C)/high temperature (HT) (600 °C) approach with thermal cycling under H₂ (between 650 and 850 °C) was used to minimize the threading dislocation density (TDD) in the Ge buffers and to have rather smooth, slightly cross-hatched surfaces.²⁵ A Siconi™ surface treatment was performed on Ge/Si pseudo-substrates and Si substrates in a dedicated chamber connected to the III–V cluster tool to remove any remaining oxides from the surface. Si substrates were then annealed in the MOCVD reactor under H₂ at high temperatures (800–900 °C) and high pressure (near atmospheric pressure) to have the formation, on the surface, of bi-atomic step edges²⁴ and avoid APB formation in the GaAs layers on top. Meanwhile, the surfaces of Ge/Si pseudo-substrates were prepared, thanks to 750 °C H₂ anneals lasting 2 min.²⁶

PIN diodes were grown in the MOCVD chamber, with ultra-pure H₂ as the carrier gas and trimethylgallium (TMGa), trimethylaluminum (TMAI), trimethylindium (TMIIn), and tertiarybutylarsine (TBAs) as group III and V precursors. The starting *n*-type doped GaAs layers were grown in two steps: 40 nm thick nucleation layers were deposited at low temperatures (LT, 400–500 °C) followed by the growth of 370 nm thick GaAs layers at high temperatures (HT, 600–700 °C).²⁷ *n*-type doping was achieved with disilane as the *n*-type precursor, with a molecular flow of 1 μmol/min of Si resulting in a doping level of $2 \times 10^{18} \text{ cm}^{-3}$. Then, twelve 10 nm thick In_{0.18}Ga_{0.82}As quantum wells (QWs) sandwiched between thirteen 11 nm thick Al_{0.1}Ga_{0.9}As barrier layers were grown at 580 °C. Finally, 52 nm thick *p*-type GaAs layers were grown on top, also at 580 °C, with diethylzinc (DEZn) as the *p*-type dopant source. The doping level of those *p*-GaAs layers was $1 \times 10^{19} \text{ cm}^{-3}$, yielding good Ohmic metal/semiconductor contacts.

To fabricate vertical PIN photodiodes, epitaxial structures were etched into circular mesas with diameters ranging from 5 to 100 μm. Mesa sidewalls were passivated with 150 nm of SiN deposited by PECVD, and Ni/Ge/Au stacks were evaporated to form the *n*-type and *p*-type metal contacts. Top view Scanning Electron Microscopy (SEM) images of the PIN photodiodes are shown in Fig. 1(b), with a zoomed-in view of the active region of a 90 μm diameter mesa.

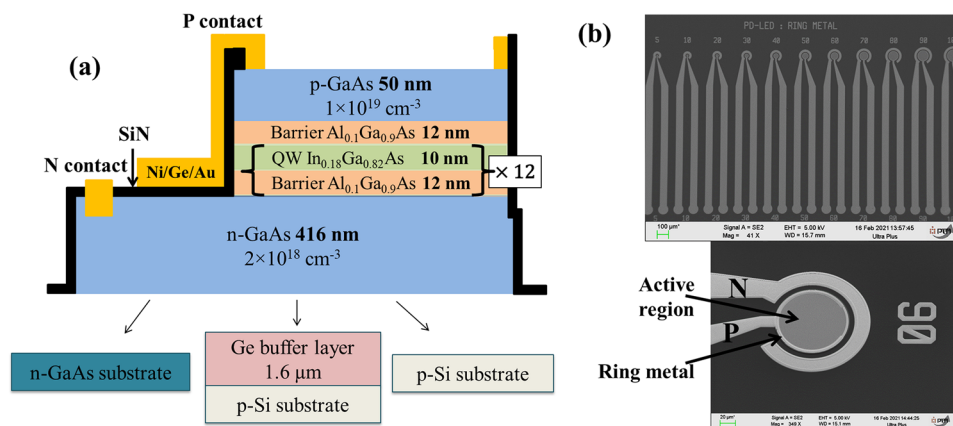


FIG. 1. (a) Schematic diagram of MQW In_{0.18}Ga_{0.82}As/Al_{0.1}Ga_{0.9}As PIN photodiodes grown on GaAs, Ge/Si, and Si substrates. (b) Top view SEM image of photodiodes with different mesa diameters and (bottom) zoomed-in view of the active region of a 90 μm diameter mesa photodiode.

III. CHARACTERISTICS AND DISCUSSIONS

Cross-sectional scanning TEM images of the MQW PIN structures grown on GaAs, Ge/Si, and Si substrates are provided in Figs. 2(a)–2(c), respectively. A high resolution cross-sectional TEM image of the MQW on the Si substrate is shown in Fig. 2(f), with a thickness of 10 nm (11 nm) for the $\text{In}_{0.18}\text{Ga}_{0.82}\text{As}$ quantum well (the $\text{Al}_{0.1}\text{Ga}_{0.9}\text{As}$ barrier). Figure 2(a) shows the high structural quality of MQWs grown on GaAs. On Ge/Si pseudo-substrates, MQWs are free of extended defects (such as APBs) and threading dislocations (TDs) on a $2\ \mu\text{m}$ wide TEM lamella, as shown in Fig. 2(b). This is due to the presence of the Ge buffer. However, there is in Fig. 2(c) a high density of threading dislocations starting at the GaAs/Si interface and propagating through the MQW when growing directly on Si. Threading Dislocation Densities (TDDs) in the PIN structures grown on Ge/Si and directly on Si were quantified with the electron channeling contrast imaging (ECCI) technique [Figs. 2(d) and 2(e)].

The TDD was reduced by nearly two orders of magnitude, from $1.8 \times 10^9\ \text{cm}^{-2}$ down to $4 \times 10^7\ \text{cm}^{-2}$, when $1.6\ \mu\text{m}$ thick Ge buffers were used.

Figures 3(a)–3(c) show micro-photoluminescence (μPL) spectra of $\text{In}_{0.18}\text{Ga}_{0.82}\text{As}/\text{Al}_{0.1}\text{Ga}_{0.9}\text{As}$ MQWs on the three types of substrates for various temperatures in the 4.5–290 K range. Figure 3(d) shows the energy shifts of the MQW signals with the measurement temperature. Above 50 K, the red shift is due to bandgap shrinkage induced by temperature (thermal activation of carriers). Experimental bandgap variations with the temperature are properly accounted for using Varshni's equation²⁸ provided in the inset of Fig. 3(d). Fitting parameters are listed in Table I. They are consistent with the values given in Ref. 29. From 4.5 to 50 K, the MQW peak position on the GaAs substrate remains constant at 1.338 eV, while those on Ge/Si and Si substrates experience a blue shift by 2.8 and 4.1 meV, respectively. It might be due to trapping of carriers in low energy

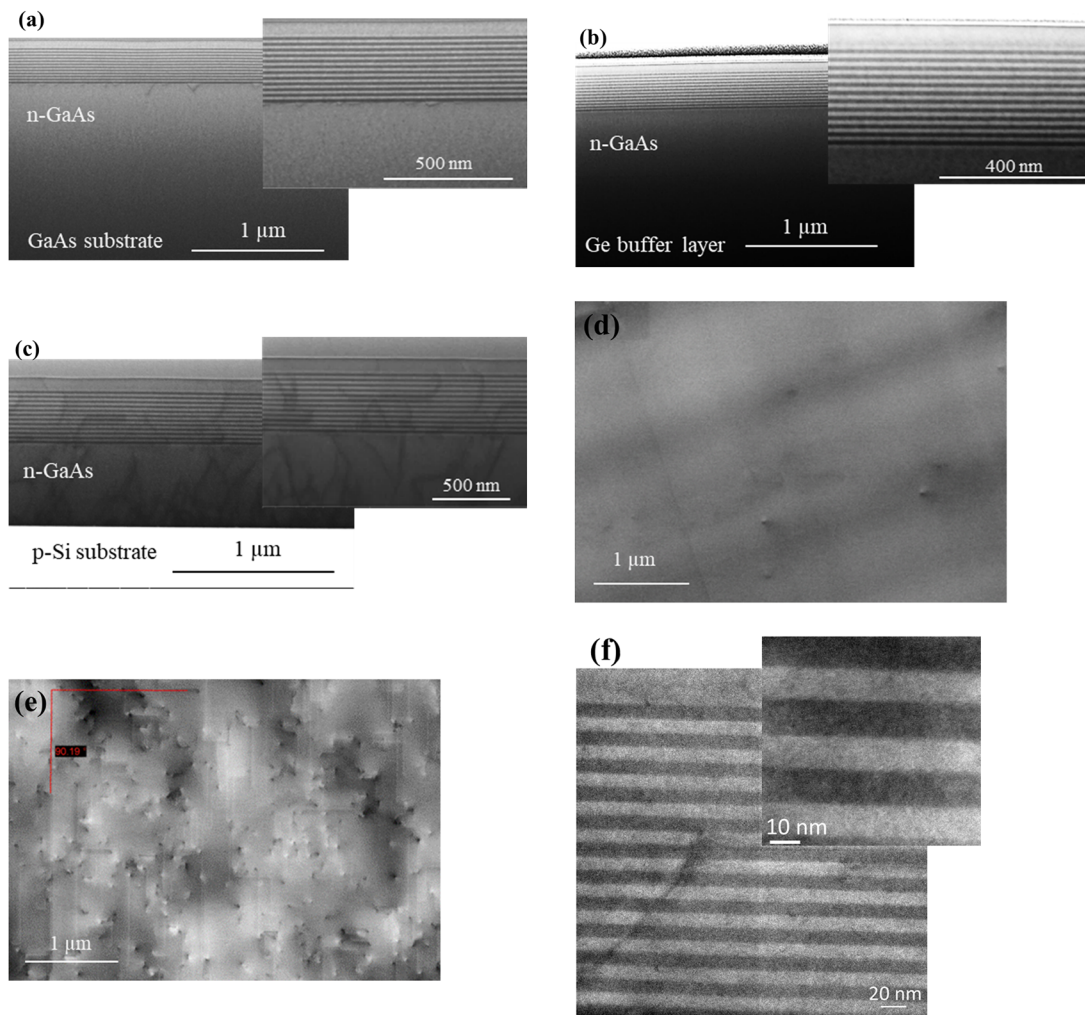


FIG. 2. High-resolution cross-sectional bright-field STEM images of MQW PIN structures grown on (a) GaAs, (b) Ge/Si, and (c) Si substrates. Top-view ECCI images of the PIN structures on (d) Ge/Si and (e) Si substrates and (f) high-resolution TEM image of the MQW on the Si substrate.

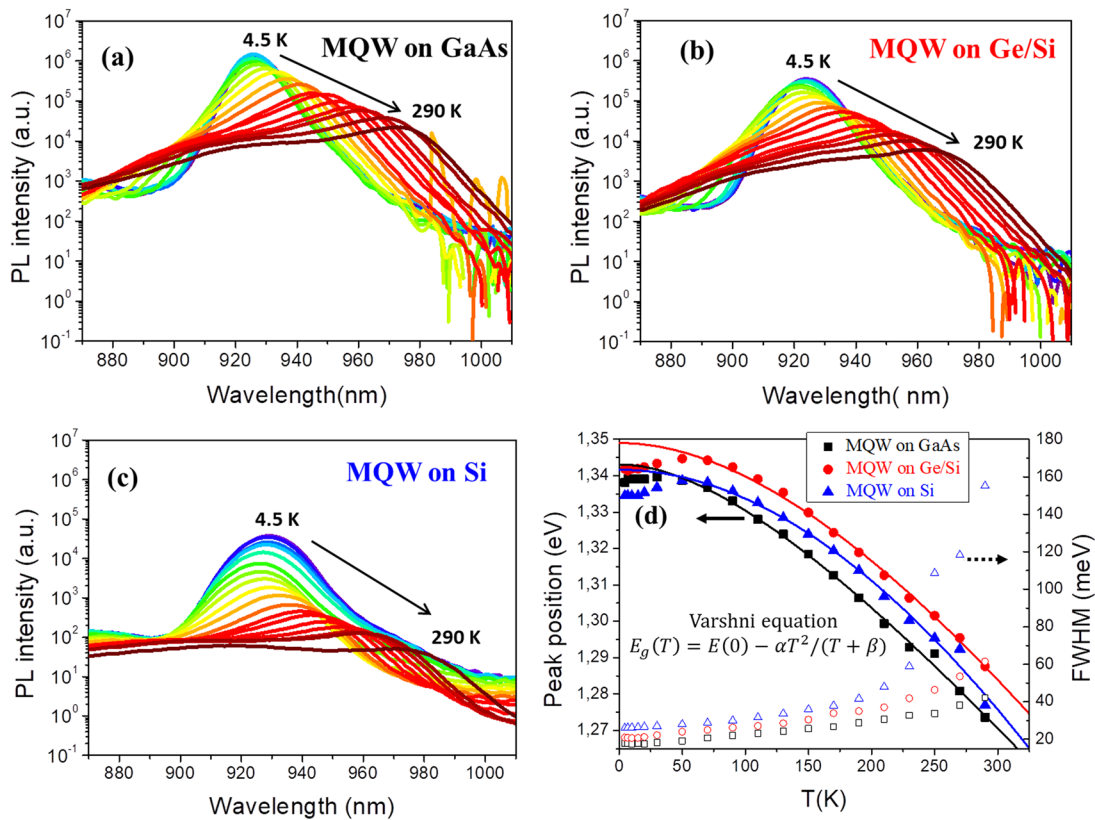


FIG. 3. PL spectra at different temperatures ranging from 4.5 to 290 K for MQWs grown on (a) GaAs, (b) Ge/Si, and (c) Si substrates, with an excitation power density of 1146 W/cm^2 . (d) Experimental transition energy (full symbols) and FWHM (empty symbols) as a function of temperature. Curves are fittings with Varshni's equation.

localized states because of the presence of structural defects in epilayers grown on Si and Ge/Si. As the temperature increases, carriers are thermally activated and redistributed in different localized states via hopping transport. Above 50 K at high temperatures, the PL emissions are dominated by carriers on delocalized states and the dependence of PL peak energy follows Varshni's expression. The full width at half maximum (FWHM) increases slowly with the temperature up to 50 K, the turning point from blue shift to red shift. Then, it increases as the temperature increases, in agreement with the classical optical phonon broadening. The FWHM at 290 K increases from 42 meV for the MQW on GaAs up to 61 and 155 meV for those on Ge/Si and Si, respectively. Such a trend is in agreement with the high TDDs in MQWs grown on Ge/Si and especially Si.

TABLE I. Values of the fitting parameters used to describe, thanks to Varshni's equation, the MQW bandgap shrinkage shown in Fig. 3(d).

Sample	E_0 (eV)	α (meV K^{-1})	β (K)
MQW on GaAs	1.343	0.44	249
MQW on Ge/Si	1.348	0.66	635
MQW on Si	1.341	1.84	2215

Figure 4(a) shows the temperature dependence of integrated PL intensity for MQWs on the various types of substrates. The integrated PL intensities decrease significantly as the temperature increases from 4.5 up to 290 K. This is due to the thermal quenching of integrated PL intensities by phonon-assisted non-radiative recombinations. These intensities can be fitted with the modified Arrhenius formula given in Eq. (1) assuming that there are two non-radiative recombination processes. The first process (1) is predominant at low temperatures and the second (2) at high temperatures,

$$I(T) = \frac{I_0}{1 + \gamma_1 e^{-\frac{E_{a(1)}}{k_B T}} + \gamma_2 e^{-\frac{E_{a(2)}}{k_B T}}}, \quad (1)$$

where I_0 is the PL intensity at 4.5 K, $E_{a(1,2)}$ are the activation energies of the non-radiative recombination processes, $\gamma_{1,2}$ are rate constants, and k_B is Boltzmann's constant. Fitting parameters are displayed in Table II. The first quenching mechanism [characterized by $E_{a(1)}$] is attributed to the delocalization of excitons coming from potential fluctuation in the $\text{In}_{0.18}\text{Ga}_{0.82}\text{As}$ wells. In our case, InGaAs QWs are 10 nm thick. Potential variations are therefore mainly due to the $\text{In}_{0.18}\text{Ga}_{0.82}\text{As}/\text{Al}_{0.1}\text{Ga}_{0.9}\text{As}$ interfacial roughness. We found small values between 1.9 and 3.9 meV for $E_{a(1)}$, indicating that the localized energy caused by interface roughness is small, in line with the abrupt MQW interfaces evidenced in TEM. $E_{a(2)}$ values are 20,

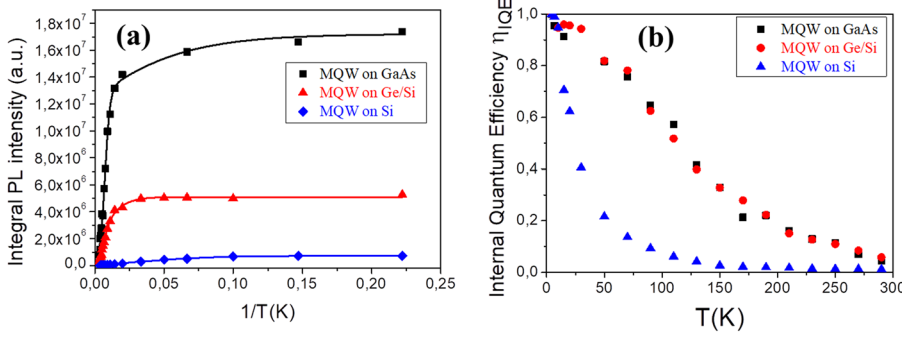


FIG. 4. (a) Temperature dependence of the integrated PL intensity for MQWs on the various types of substrates and (b) relative internal quantum efficiency (η_{IQE}) evolution as a function of temperature.

41, and 45 meV for MQWs on Si, Ge/Si, and GaAs, respectively. ECCI measurements showed the lowest TDD values for MQWs on GaAs and a definite TDD reduction for MQWs on Ge/Si substrates instead of bare Si. $E_{a(2)}$ therefore increases as the TDD decreases. This may result from the suppression of non-radiative recombination centers linked to threading dislocations. We believe that a reduced TDD leads to a higher activation energy for exciton quenching. Higher $E_{a(2)}$ values because of lower TDD are associated with improved internal quantum efficiencies (IQEs), as we will see in the following.

Let us assume that the internal quantum efficiency (η_{IQE}) is 100% at 4.5 K, with a maximum integrated PL intensity $I(T_0)$. η_{IQE} can then be extracted by calculating the ratio $I(T)/I(T_0)$, where $I(T)$ is the integrated PL intensity at temperature T. As shown in Fig. 4(b), the η_{IQE} evolution vs temperature is similar for GaAs and Ge/Si substrates. However, the η_{IQE} for MQW on Si decreases rapidly between 4.5 and 100 K. Above this temperature, its value is close to zero. This comparison shows how high numbers of threading dislocations drastically degrade the MQW emission efficiency.

Figure 5(a) shows the dark current voltage (I - V) curves measured at 300 K using a 4155C Agilent semiconductor parameter analyzer for photodiodes with 90 μm mesa diameters on the three types of substrates. Photodiodes on Ge/Si and GaAs exhibit low dark currents of 1.9 and 1.4 nA under a bias voltage of -3 V, corresponding to dark current densities of 2.5×10^{-5} and 1.8×10^{-5} A/cm², respectively. These values are lower by one order of magnitude than the dark current density for an InAs/InGaAs quantum dot p - i - n photodiode grown on GaP/Si.³⁰ This is likely due to the high crystalline quality of the epilayers. However, the photodiode on Si has a definitely higher dark current. It is, for example, 12 nA at -3 V, resulting in a dark current density of 1.6×10^{-4} A/cm². This is consistent with the TDD in MQWs on Si, which is almost two orders of magnitude higher than on Ge/Si. Figure 5(b) shows the evolution of the dark current with the mesa diameter at three forward bias values of 0.7, 0.6, and 0.5 V for PDs on GaAs. Clearly, the dark current increases

with the mesa size. A fit of the dark current by the equation provided in the inset of Fig. 5(b) yields the bulk current density, J_{bulk} , which is linked to the epitaxial stack quality, and the sidewall current density, J_{sidewall} , also known as the perimeter or peripheral dark current

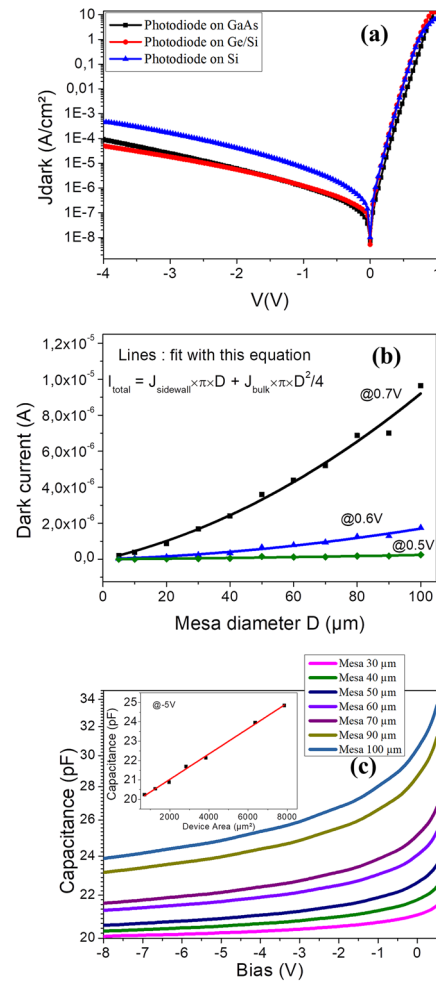


FIG. 5. (a) Current–voltage characteristics of 90 μm mesa diameter photodiodes on GaAs, Ge/Si, and Si substrates. (b) Dark current vs mesa diameter at three forward bias values, 0.7, 0.6, and 0.5 V, for a photodiode on GaAs. Curves are fits with the equation given in the inset. (c) Capacitance voltage characteristics of photodiodes with different mesa diameters on GaAs. Inset: measured capacitance of a set of photodiodes under a bias of -5 V.

TABLE II. Values of the fitting parameters used to describe, thanks to Eq. (1) modified Arrhenius formula, the integral PL intensity evolution as a function of $(1/T)$.

Sample	I_0	γ_1	$E_{a(1)}$ (meV)	γ_2	$E_{a(2)}$ (meV)
MQW on GaAs	17 130 650	0.38	1.9	72	45
MQW on Ge/Si	5 153 819	0.58	3.8	50	41
MQW on Si	722 379	5.70	3.4	129	20

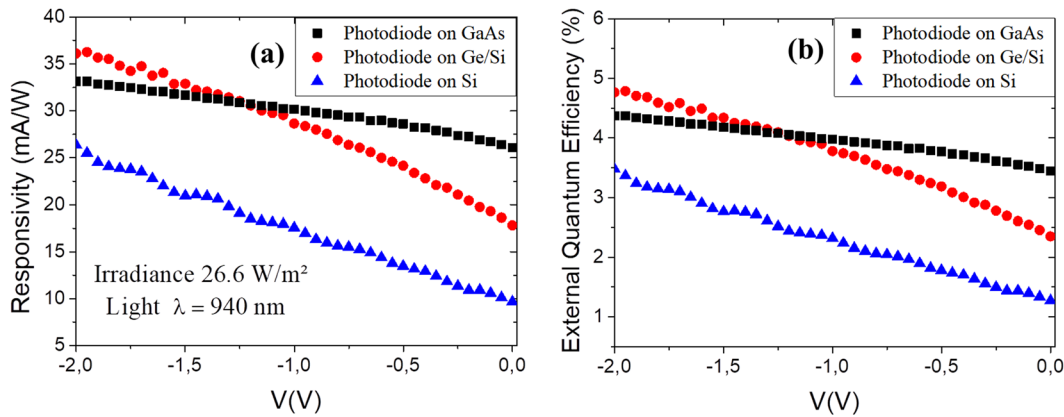


FIG. 6. (a) Average bias voltage dependence of the room temperature resistivities upon 26.6 W/m² irradiance at 940 nm. Mean data from 14 photodiodes with mesa diameters of 90 μm on GaAs, Ge/Si, and Si substrates. (b) Corresponding external quantum efficiencies (EQEs).

density, which depends on the device fabrication scheme and its imperfections (i.e., mesa etching, sidewall passivation, etc.). Regardless of the forward bias value, J_{sidewall} was higher than J_{bulk} by at least one order of magnitude. At 0.7 V, J_{sidewall} and J_{bulk} were, for instance, 1.2×10^{-8} and 6.5×10^{-10} A/cm². This meant that mesa etching and sidewall passivation processes should be improved.

The capacitance voltage (C-V) characteristics of photodiodes were also measured at 300 K, as shown in Fig. 5(c), with a 4294A Agilent impedance analyzer. A capacitance of 19.7 pF was extracted from the capacitance vs device area curve in the inset of Fig. 5(b). Such high values are likely due to the thin intrinsic region thickness (~263 nm) resulting in a low transit time, limiting the bandwidth for large diameter PDs. One possible way to reduce the capacitance value could be to increase the thickness of that region, which would amplify the transit time. In the future, the RC delay and the transit time will be evaluated to improve the PD structure.

The optical responses were measured using a Cascade Elite 300 prober equipped with a 940 nm LED light source having an irradiance of 26.6 W/m² and a B1500 semiconductor analyzer. Figure 6(a) shows the 300 K average responsivity evolution of 14 photodiodes with 90 μm mesa diameters vs reverse bias voltage on each type of substrate. Clearly, the responsivity always increases with the reverse bias voltage for all photodiodes. A higher electric field is then generated, resulting in the extraction of more photo-carriers. Photodiodes on GaAs have responsivities between 26 and 33 mA/W, always higher than the ones on Si regardless of the reverse bias value. Unexpectedly, at high reverse bias above -1.2 V, PDs on Ge/Si have a responsivity value higher than those on GaAs. This is likely due to a shift of the absorption edge for MQWs when moving from GaAs to Ge/Si or Si substrates. More investigation is needed to clarify this. The corresponding external quantum efficiency (EQE) is given in Fig. 6(b), with 4.3%, 4.7%, and 3.4% values at -2 V for photodiodes on GaAs, Ge/Si, and Si substrates, respectively. At higher reverse bias of -4 V, the EQE of these photodiodes could reach 8%. These low values are mainly explained by the small thickness of the absorption layer (~120 nm). We then used the EQE to calculate the specific detectivity

$$D^* = \sqrt{q} \frac{\lambda \cdot \eta}{hc \sqrt{2J_{\text{dark}}}}, \quad (2)$$

where η is the external quantum efficiency (EQE) and J_{dark} is the dark current density (A/cm²). Numerical calculations gave 2.4×10^{10} , 2.9×10^{10} , and 8.5×10^9 cm²√Hz W⁻¹ detectivities at -2 V for MQW devices on GaAs, Ge/Si, and Si substrates, respectively. Such stacks could advantageously be used in a lateral configuration for photonic integrated circuits suitable for ultra-fast optical communication with all devices fabricated from III-V semiconductors.^{7,8,31,32}

IV. CONCLUSION

In conclusion, we fabricated vertical PIN MQW InGaAs/AlGaAs PDs. The III-V stacks at the heart of those devices were epitaxially grown on GaAs(001) and on 300 mm diameter bare and Ge-buffered Si(001) substrates. A low dark current density of 2.5×10^{-5} A/cm² was obtained on Ge/Si substrates, highlighting the potential of such templates. In the future, we will keep the same PIN stack and use a lateral current collection (LCC) configuration, providing a decoupling between the carrier collection and the light propagation directions. This should yield a high near infrared bulk absorption with low capacitance, low leakage current, and low dark current with very thin PDs. Threading dislocations in the PIN stacks stemming from the use of lattice-mismatched substrates had an impact on MQW photoluminescence. A better understanding of the impact of threading dislocations on emitter and collector performances should help in paving the way for a monolithic integration of III-V devices by direct epitaxy on Si, replacing the complex and costly wafer bonding techniques.

ACKNOWLEDGMENTS

This work was partially supported by the French “Recherches Technologiques de Base” (Basis Technologies Research), RENATECH programs, and the French National Research Agency in the framework of the Investissements d’Avenir Program (Grant Nos. ANR-10-IRT-05 and ANR-15-IDEX-02). The authors want to thank

the CEA Leti clean staff, the Nanocharacterization Platform (PFNC), and Applied Materials for technical assistance on the MOCVD tool and fruitful discussions.

DATA AVAILABILITY

The data that support the findings of this study are available within the article.

REFERENCES

- ¹L. C. West and S. J. Eglash, *Appl. Phys. Lett.* **46**, 1156 (1985).
- ²X. Li, S. Ni, Y. Jiang, J. Li, W. Wang, J. Yuan, D. Li, X. Sun, and Y. Wang, *ACS Omega* **6**, 8687–8692 (2021).
- ³F. D. P. Alves, G. Karunasiri, N. Hanson, M. Byloos, H. C. Liu, A. Bezinger, and M. Buchanan, *Infrared Phys. Technol.* **50**, 182 (2007).
- ⁴A. Bezinger, H. C. Liu, B. Aslan, M. Buchanan, A. J. Springthorpe, P. J. Poole, D. A. Cardimona, and G. J. Brown, *Electron. Lett.* **43**, 685 (2007).
- ⁵R. Thakur, "Infrared sensors for autonomous vehicles," in *Recent Development in Optoelectronic Devices*, edited by R. Srivastava (IntechOpen (InTech), 2017), p. 84.
- ⁶Y. Wan, Z. Zhang, R. Chao, J. Norman, D. Jung, C. Shang, Q. Li, M. J. Kennedy, D. Liang, C. Zhang, J.-W. Shi, A. C. Gossard, K. May Lau, and J. E. Bowers, *Opt. Express* **25**, 27715 (2017).
- ⁷B. Chen, Y. Wan, Z. Xie, J. Huang, N. Zhang, C. Shang, J. Norman, Q. Li, Y. Tong, K. May Lau, A. C. Gossard, and J. E. Bowers, *ACS Photonics* **7**, 528 (2020).
- ⁸J. Huang, Y. Wan, D. Jung, J. Norman, C. Shang, Q. Li, K. May Lau, A. C. Gossard, J. E. Bowers, and B. Chen, *ACS Photonics* **6**, 1100 (2019).
- ⁹S. Mauthe, Y. Baumgartner, S. Sant, Q. Ding, M. Sousa, and L. Czornomaz, in *Optical Fiber Communication Conference (OFC), OSA Technical Digest* (Optical Society of America, 2020), paper M3D3.
- ¹⁰K. Sun, D. Jung, C. Shang, A. Liu, J. Morgan, J. Zang, Q. Li, J. Klamkin, J. E. Bowers, and A. Beling, *Opt. Express* **26**, 13605 (2018).
- ¹¹N. Hong, R. J. Chu, S. S. Kang, G. Ryu, J.-H. Han, K. J. Yu, D. Jung, and W. J. Choi, *Opt. Express* **28**, 36559 (2020).
- ¹²B. Pezeshki, S. M. Lord, and J. S. Harris, *Appl. Phys. Lett.* **59**, 888 (1991).
- ¹³L. Buydens, P. Demeester, and P. Van Daele, *Opt. Quantum Electron.* **24**, S167 (1992).
- ¹⁴D. Mahgerefteh, C. M. Yang, L. Chen, K. Hu, W. Chen, E. Garmire, and A. Madhukar, *Appl. Phys. Lett.* **61**, 2592 (1992).
- ¹⁵R. Mariella, J. Morse, and Z. Liliental-Weber, *MRS Online Proc. Libr.* **198**, 297 (1990).
- ¹⁶O. Sjölund, M. Ghisoni, and A. Larsson, *IEEE J. Quantum Electron.* **33**, 1323 (1997).
- ¹⁷M. Zirngibl and M. Ilegems, *J. Appl. Phys.* **69**, 8392 (1991).
- ¹⁸A. C. Farrell, X. Meng, D. Ren, H. Kim, P. Senanayake, N. Y. Hsieh, Z. Rong, T.-Y. Chang, K. M. Azizur-Rahman, and D. L. Huffaker, *Nano Lett.* **19**, 582 (2019).
- ¹⁹F. D. P. Alves, R. A. T. Santos, L. F. M. Nohra, L. B. Magalhães, and G. Karunasiri, in *2009 SBMO/IEEE MTT-S International Microwave and Optoelectronics Conference (IMOC), Belem, Brazil* (IEEE, 2009), Vol. 8, p. 303.
- ²⁰D. S. Katzer, W. S. Rabinovich, K. Ikossi-Anastasiou, and G. C. Gilbreath, *J. Vac. Sci. Technol. B* **18**, 1609 (2000).
- ²¹N. Baidus, V. Aleshkin, A. Dubinov, K. Kudryavtsev, S. Nekorkin, A. Novikov, D. Pavlov, A. Rykov, A. Sushkov, M. Shaleev, P. Yunin, D. Yurasov, and Z. Krasilnik, *Crystals* **8**, 311 (2018).
- ²²V. Ya. Aleshkin, N. V. Baidus, A. A. Dubinov, A. G. Fefelov, Z. F. Krasilnik, K. E. Kudryavtsev, S. M. Nekorkin, A. V. Novikov, D. A. Pavlov, I. V. Samartsev, E. V. Skorokhodov, M. V. Shaleev, A. A. Sushkov, A. N. Yablonskiy, P. A. Yunin, and D. V. Yurasov, *Appl. Phys. Lett.* **109**, 061111 (2016).
- ²³Y. Han and K. May Lau, *J. Appl. Phys.* **128**, 200901 (2020).
- ²⁴M. Martin, D. Caliste, R. Cipro, R. Alcotte, J. Moeyaert, S. David, F. Bassani, T. Cerba, Y. Bogumilowicz, E. Sanchez, Z. Ye, X. Y. Bao, J. B. Pin, T. Baron, and P. Pochet, *Appl. Phys. Lett.* **109**, 253103 (2016).
- ²⁵Y. Bogumilowicz, J. M. Hartmann, N. Rochat, A. Salaun, M. Martin, F. Bassani, T. Baron, S. David, X.-Y. Bao, and E. Sanchez, *J. Cryst. Growth* **453**, 180 (2016).
- ²⁶J. M. Hartmann, A. Abbadie, A. M. Papon, P. Holliger, G. Rolland, T. Billon, J. M. Fédéli, M. Rouvière, L. Vivien, and S. Laval, *J. Appl. Phys.* **95**, 5905 (2004).
- ²⁷R. Alcotte, M. Martin, J. Moeyaert, R. Cipro, S. David, F. Bassani, F. Ducroquet, Y. Bogumilowicz, E. Sanchez, Z. Ye, X. Y. Bao, J. B. Pin, and T. Baron, *APL Mater.* **4**, 046101 (2016).
- ²⁸Y. P. Varshni, *Physica* **34**, 149 (1967).
- ²⁹D. K. Gaskill, N. Bottka, L. Aina, and M. Mattingly, *Appl. Phys. Lett.* **56**, 1269 (1990).
- ³⁰D. Inoue, Y. Wan, D. Jung, J. Norman, C. Shang, N. Nishiyama, S. Arai, A. C. Gossard, and J. E. Bowers, *Appl. Phys. Lett.* **113**, 093506 (2018).
- ³¹Y. Baumgartner, M. Seifried, C. Caer, P. Stark, D. Caimi, J. Faist, B. J. Offrein, and L. Czornomaz, in *Optical Fiber Communication Conference (OFC), OSA Technical Digest* (Optical Society of America, 2019), paper M3D3.
- ³²Z. Sheng, L. Liu, J. Brouckaert, S. He, and D. Van Thourhout, *Opt. Express* **18**, 1756 (2010).